ACS APPLIED NANO MATERIALS

www.acsanm.org

Article

Exfoliated Polymeric Carbon Nitride Nanosheets for Photocatalytic Applications

Junhao Huang, Marcus Klahn, Xinxin Tian, Xingchao Dai, Jabor Rabeah, Victoria Aladin, Björn Corzilius, Stephan Bartling, Henrik Lund, Norbert Steinfeldt, Tim Peppel, Andrew J. Logsdail, Haijun Jiao, and Jennifer Strunk*

Cite This: https://doi.org/10.1021/acsanm.4c00133

Read Online

ACCESS | Metrics & More | Article Recommendations | Supporting Information

ABSTRACT: Exfoliation into a 2D nanosheet structure can lead to enhanced surface activity and unique optical and electronic properties in polymeric carbon nitride (PCN). In this study, four common exfoliation strategies (liquid ultrasonication, thermal oxidation, hydrothermal oxidation, and chemical oxidation) were adopted, and their effects on the structural and electronic changes in PCN were analyzed in detail. This allows us to understand the relationship between the exfoliation mechanism and the structural/optical properties. Here, we demonstrate that the thermal and ultrasonic exfoliation methods can effectively reduce the thickness of PCN while preserving its original structure. In contrast, the chemical and hydrothermal treatments can strongly affect the morphology and structure of PCN, leading to a decreased performance in phenol photodegradation. Therefore, depending on the employed exfoliation method, the surface area, functionalization, band edge positions, charge carrier generation, and mobility are influenced differently up to the point where semiconducting behavior is entirely lost. Our results allow conclusions about the applicability of the different exfoliation methods to obtain distinct material properties for photocatalytic applications.

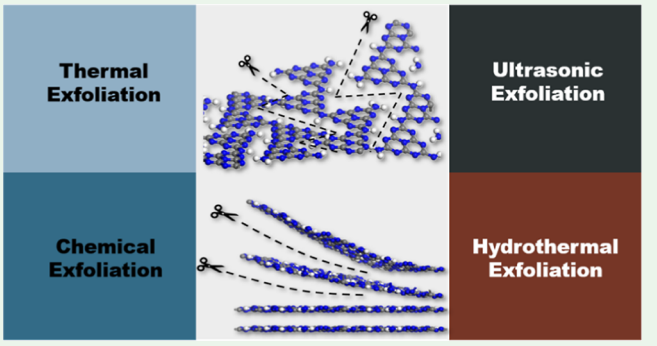

KEYWORDS: *polymeric carbon nitride, exfoliation, nanosheet, hydrogen bond, π−π interaction, photocatalysis*

INTRODUCTION

Polymeric carbon nitride (PCN) is considered a desirable photocatalytic material because of the abundant raw materials and a suitable optical bandgap of 2.7 eV.[1,2] Numerous photocatalytic reactions have been reported with PCN, such as CO_2 photoreduction,[3−5] water splitting,[6−8] pollutant photodegradation,[9−11] and selective synthesis of organic compounds.[12] However, due to the limited light absorption ability, coupled with the rapid recombination rate of photoinduced electron−hole pairs and low surface area, the photocatalytic performance of unmodified PCN is poor and unsatisfactory for industrial applications.[13,14]

The fast development of exfoliation technologies for two-dimensional (2D) materials offers a possibility to enhance the photoactivity of PCN.[15] Exfoliation enables the conversion of three-dimensional materials into a 2D structure, with optical and electronic properties that change greatly from those of the pristine counterpart due to the quantum confinement of electrons. The most typical example is graphite,[16] where exfoliation into a monolayer or a few layers of graphene gives a wide range of different electronic, optical, mechanical, and electrochemical properties. Motivated by the discovery of graphene, a number of exfoliation methods have been adopted to produce atomically thin PCN nanosheets, such as thermal oxidation method,[17] liquid-assisted ultrasonic method,[18] hydrothermal oxidation method,[19] and chemical oxidation method.[20] Several special methods have also been reported, like the melamine-assisted method,[21] steam reforming method,[22] and mechanical grinding method.[23]

Notably, different exfoliation methods have distinct effects on the morphology and electronic structure of PCN.[24] For liquid-assisted ultrasonic exfoliation, the acoustic energy of ultrasonic wave is transmitted to overcome the van der Waals forces between the layers to obtain the nanosheets.[25,26] Thermal oxidation etching of pristine PCN in air was first reported by Niu et al. in 2012.[17] The in-plane hydrogen bonds between the adjacent strands of polymeric melon units are destroyed by the oxidation processes in air, which leads to a

Received: January 8, 2024
Revised: March 15, 2024
Accepted: March 16, 2024

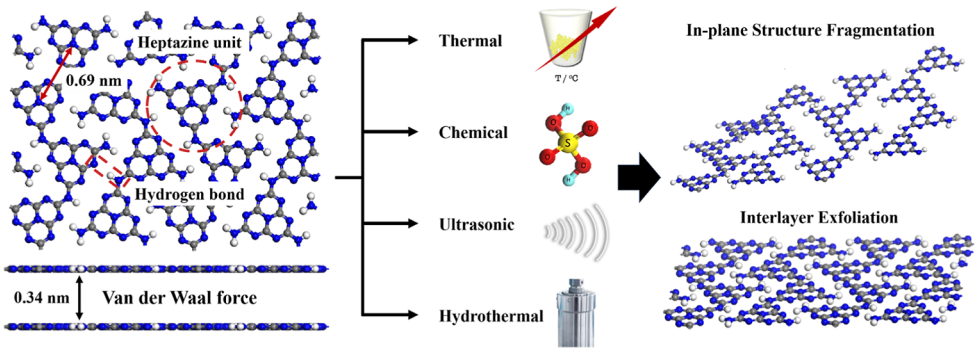

Figure 1. Schematic illustration of different exfoliation processes for synthesizing nanolayered PCN.

gradual decrease in the thickness of pristine PCN, achieving nanoscale range through a layer-by-layer thermal etching process. Additionally, inspired by graphene oxide, the treatment of PCN with oxidizers, such as H_2SO_4, results in the addition of hydroxyl and epoxide groups to the basal plane.[27] The delamination mechanism in concentrated H_2SO_4 is mediated by its oxidation and protonation effect, along with the exothermic effect after mixing with H_2O. These effects facilitate the cleavage of hydrogen bonds and structural defects in PCN to produce small-sized fragments. Thus, PCN nanosheets can be obtained via a range of methods, which are suspected to result in a variety of physicochemical properties, such as surface area, optical/electronic properties, surface groups, structural defects, etc.

PCN nanosheets ideally consist of only single monolayers, but they are often manifested as incompletely exfoliated flakes comprising a small number (<10) of stacked monolayers.[28] Previous studies have utilized high-speed centrifugation to separate nanosheets from large particles; however, the principle of the method relies on mass rather than thickness.[18,25] As a result, the final centrifuged PCN still contained a mixture of nanosheets and small particles. Additionally, particles in their bulk counterparts exhibit varying sizes and thicknesses. When applying exfoliation to the bulk PCN, whole particle sizes will gradually decrease., i.e., large particles will exfoliate into small particles, and small particles will exfoliate into nanometer-sized moieties. The consequence of exfoliation is therefore a broader size distribution, which is inevitable.

In this work, we did not adopt a centrifugation method to separate the final product. Instead, we focus on examining the changes in properties that occur as the overall particle size decreases throughout the whole sample. Here, urea, an oxygen-containing nitrogen-rich material, was chosen as the precursor to synthesize pristine PCN through a thermal-condensation method. In comparison to alternative precursors like melamine or dicyandiamide, urea-derived PCN is usually more porous, with a thinner thickness and a higher specific surface area.[29] The PCN was then exfoliated or delaminated via four different methods: liquid ultrasonication, thermal oxidation, hydrothermal oxidation, and chemical oxidation etching (Figure 1). Through a series of characterization techniques, the differences in the exfoliated PCN are presented, considering morphology, crystal, and molecular structure, as well as optical and electronic properties.

RESULTS AND DISCUSSION

Process of Exfoliation of the Pristine PCN. Ideally, the exfoliation of PCN results in the breaking of weak interlayer van der Waals interactions and separation in a layer-by-layer manner starting from the surface layer. Such layer-by-layer exfoliation requires strong in-plane bonding via C−N covalent interactions, which are optimized with an ideal C/N ratio of 0.75. In fact, the composition of PCN is usually closer to $C_3N_{4.7}H_{1.5}$, with a hydrogen content of 1.5 wt % or more, and the hydrogen atoms exist in the form of in-plane N−H···N bond.[30] Thus, during the chemical and physical exfoliation of PCN, not only is the interlayer $\pi-\pi$ stacking broken but the in-plane hydrogen bonding is also likely to be disrupted. Here, density functional theory (DFT) calculations were conducted to study the interlayer van der Waals interactions and in-plane hydrogen bonds. We started from the interlayer van der Waals interactions and determined it by layer-by-layer exfoliation of a ten-layer hydrogen-bonding PCN model (Figure S1). The interlayer energy per atom (72 atoms: $C_{24}H_{12}N_{36}$) in the unit cell, E_a, was determined by the eq 1

$$E_a = \left(\frac{E_n - n \times E_1}{n - 1}\right)/72 \quad (1)$$

where n is the number of layers in the model (i.e., 10), E_n is the corresponding energy of the n-layer model, and E_1 is the energy of the monolayer model. The average interlayer energy E_a is calculated as −0.03 eV/atom. The value is derived by assuming that the interlayer interaction energy is equally shared among all species.

After determining the interlayer energy, we analyze now the in-plane hydrogen bonds (Figure S2). The energy of in-plane hydrogen bonds (12H atoms in one unit) for the monolayer model, $E_{N-H\cdots N}$, was determined by the eq 2

$$E_{N-H\cdots N} = [(E_{total} + ZPE_{total}) - (E_{left} + ZPE_{left}) - (E_{right} + ZPE_{right})]/12 \quad (2)$$

where E_{total} is the energy of the monolayer model, E_{left} is the corresponding energy of the left fragment of the monolayer model, and E_{right} is the corresponding energy of the right fragment of the monolayer model. The zero-point energies were determined independently for each model to determine the lowest energy state. The energy of a hydrogen bond $E_{N-H\cdots N}$ is calculated as −0.30 eV per interaction, which is significantly stronger than the interlayer van der Waals interactions. This suggests that exfoliation will only occur between the layers when the input energy is kept within the range of −0.03 to −0.30 eV. If the input energy is sustained above −0.30 eV, exfoliation will disrupt the interlayer interactions as well as the in-plane hydrogen bonds. However, at the current level of experimental exfoliation, the input

https://doi.org/10.1021/acsanm.4c00133
ACS Appl. Nano Mater. XXXX, XXX, XXX−XXX

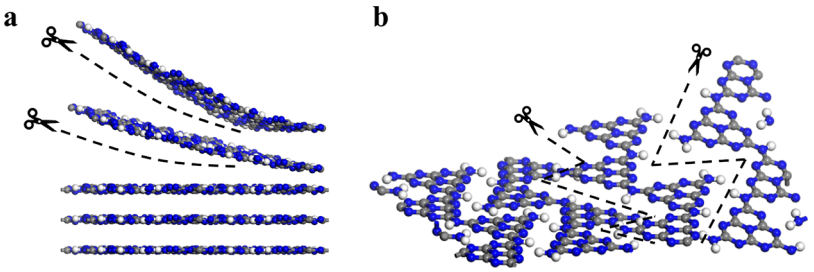

Figure 2. Two processes to reduce the size of PCN: (a) interlayer exfoliation and (b) in-plane structure fragmentation.

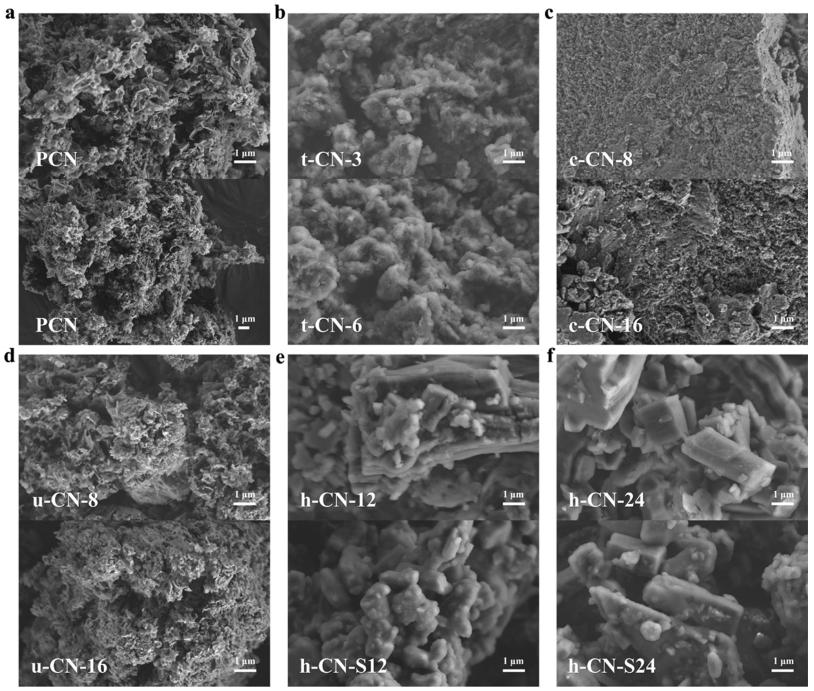

Figure 3. SEM images of PCN (a), t-CN (b), c-CN (c), u-CN (d), and h-CN (e,f).

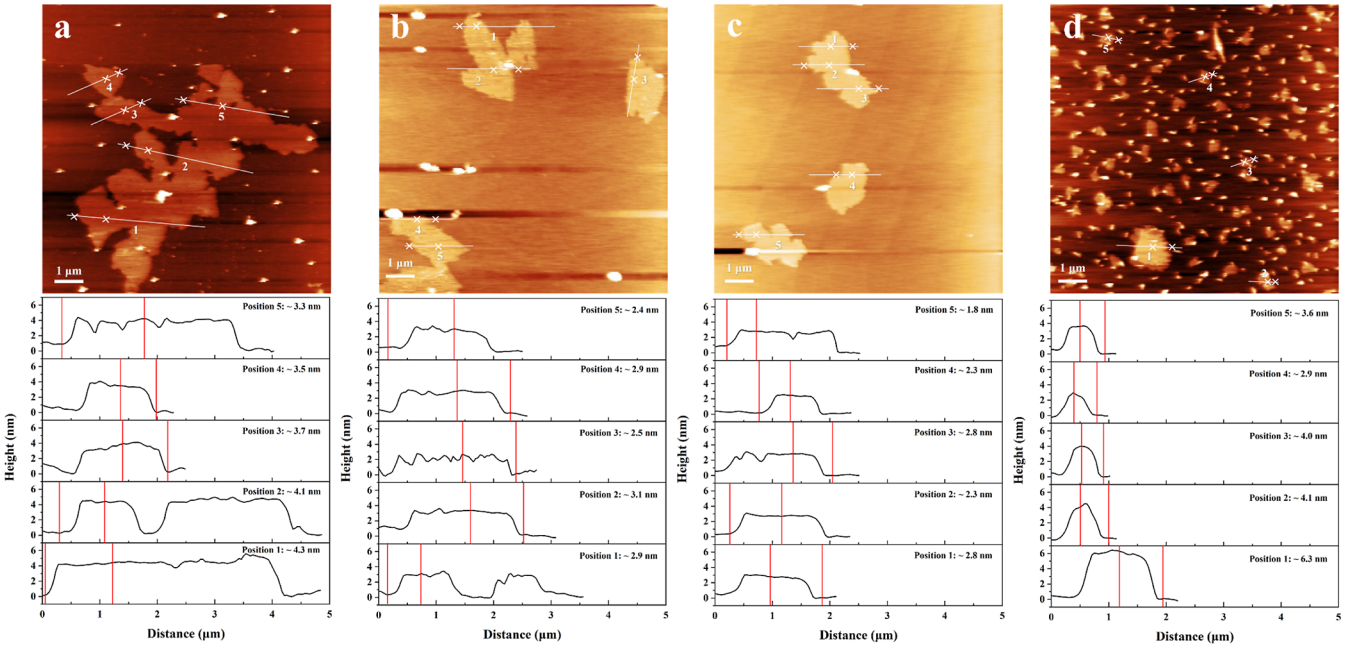

Figure 4. AFM images and corresponding height profiles of pristine PCN (a), t-CN-6 (b), u-CN-16 (c), and c-CN-16 (d).

https://doi.org/10.1021/acsanm.4c00133
ACS Appl. Nano Mater. XXXX, XXX, XXX−XXX

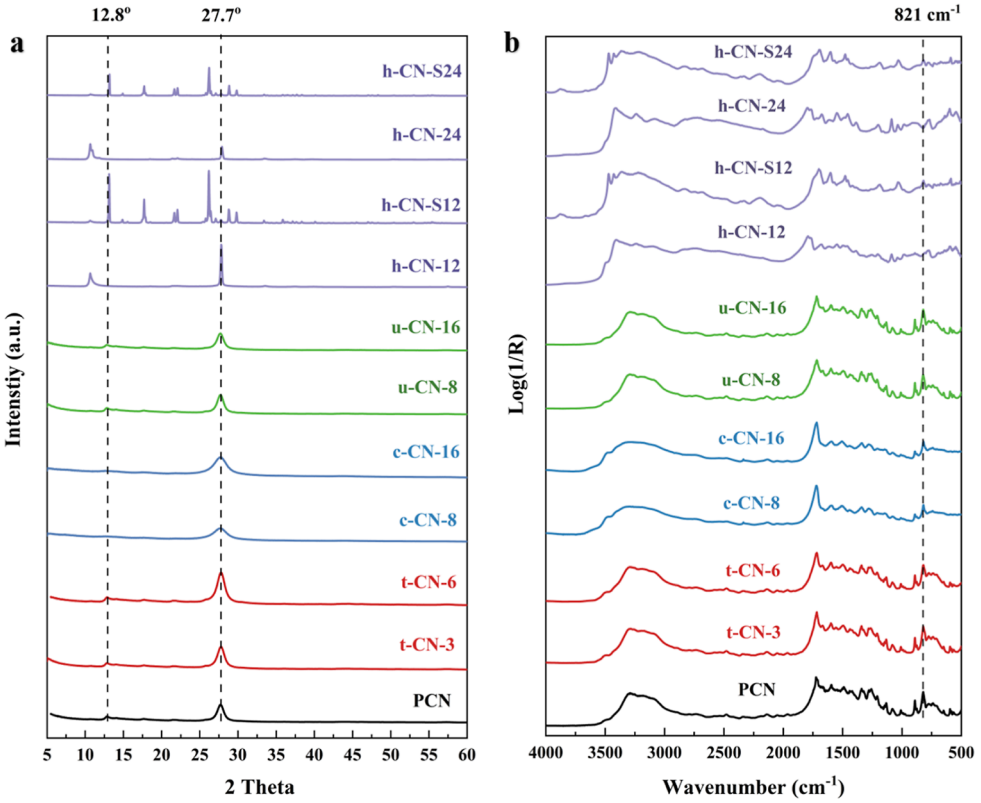

Figure 5. (a) XRD patterns and (b) DRIFTS spectra of differently exfoliated PCN.

energy transmitted through the medium to the material is difficult to control and measure; furthermore, to make sure exfoliation occurs, the input energy is usually much greater than the minimum energy required to break interlayer interactions. Therefore, two processes are expected to occur during exfoliation, as depicted in Figure 2: (i) the breaking of weaker $\pi-\pi$ interactions between the layers and (ii) the breaking of stronger in-plane hydrogen bonds between strands of heptazine units. Theoretical elucidation of the exfoliation process provides hints to help understand the structural and electronic changes obtained from the experimental characterization.

Morphology and BET Surface Area. The morphology and microstructure of exfoliated samples were investigated by scanning electron microscopy (SEM). Pristine PCN exhibited an irregular wrinkled morphology with an already thin structure (Figure 3a). After thermal oxidation exfoliation, the resulting t-CN displayed an ordered sheet-like morphology with a soft and loose structure (Figures 3b and S6b). In the case of c-CN, the wrinkled structure of PCN was fully destroyed after chemical oxidation exfoliation (Figure 3c), transforming into a dense block structure (Figures S6c and S7). No pores can be observed on its surface. The morphology of u-CN resembled that of pristine PCN, suggesting that the original morphology of PCN has been largely preserved after ultrasonication treatment. SEM images of h-CN (Figures 3e,f, and S6e,f; the water-soluble samples were referred to as h-CN-S12 and h-CN-S24) showed that the materials transformed into large rod-like structures. To sum up, thermal, chemical, and hydrothermal oxidation exfoliation strongly affected the original structure of PCN, while ultrasonic exfoliation did not.

The thickness of the exfoliated PCN was evaluated using atomic force microscopy (AFM). The average thickness of pristine PCN (Figure 4a) was determined to be 3.9 nm equivalent to approximately 13 monolayers, considering the interlayer distance in the pristine PCN of about 0.320 nm.[30] The thicknesses of t-CN-3 (Figure S8) and t-CN-6 (Figure 4b) decreased to 3.2 nm (equivalent to 11 layers) and 2.8 nm (equivalent to 10 layers), respectively. The AFM image in Figure 4c shows that the thickness of u-CN-16 is 2.4 nm (equivalent to 9 layers). The reduced thicknesses in t-CN and u-CN confirm effective exfoliation by thermal and ultrasonic treatments. A thinner nanostructure often provides materials with a greater surface area, exposing more active sites for catalytic reactions. For c-CN-16, the AFM image (Figure 4d) exhibits flakes with much smaller sizes, most up to around 0.7 μm, whereas its thickness increased to 4.2 nm (equivalent to 14 layers). This suggests that the chemical exfoliation of PCN disrupted the surface hydrogen-bonding network, causing aggregation into a block structure, consistent with the SEM observation.

Figure S9 provides quantitative details of the Brunauer–Emmett–Teller (BET) surface areas for all samples. The BET surface area of t-CN-3 is calculated to be 131 $m^2\ g^{-1}$, higher than that of pristine PCN (103 $m^2\ g^{-1}$). However, the specific surface area of t-CN-6 did not increase further but decreased to 92 $m^2\ g^{-1}$ due to the denser packing structure caused by excessive thermal exfoliation. A similar trend occurred also in the u-CN samples. The surface area of u-CN-8 is similar to pristine CN, but that of u-CN-16 decreased to 91 $m^2\ g^{-1}$. After chemical exfoliation, to our surprise, the BET surface areas of c-CN-8 and c-CN-16 plummeted to 7 and 13 $m^2\ g^{-1}$, respectively. This is due to the destruction of the porous structure caused by the oxidation effect of H_2SO_4. Similarly, the BET surface area of all h-CN samples dropped below 10 $m^2\ g^{-1}$. Therefore, except for t-CN-3, the BET surface areas of

https://doi.org/10.1021/acsanm.4c00133
ACS Appl. Nano Mater. XXXX, XXX, XXX−XXX

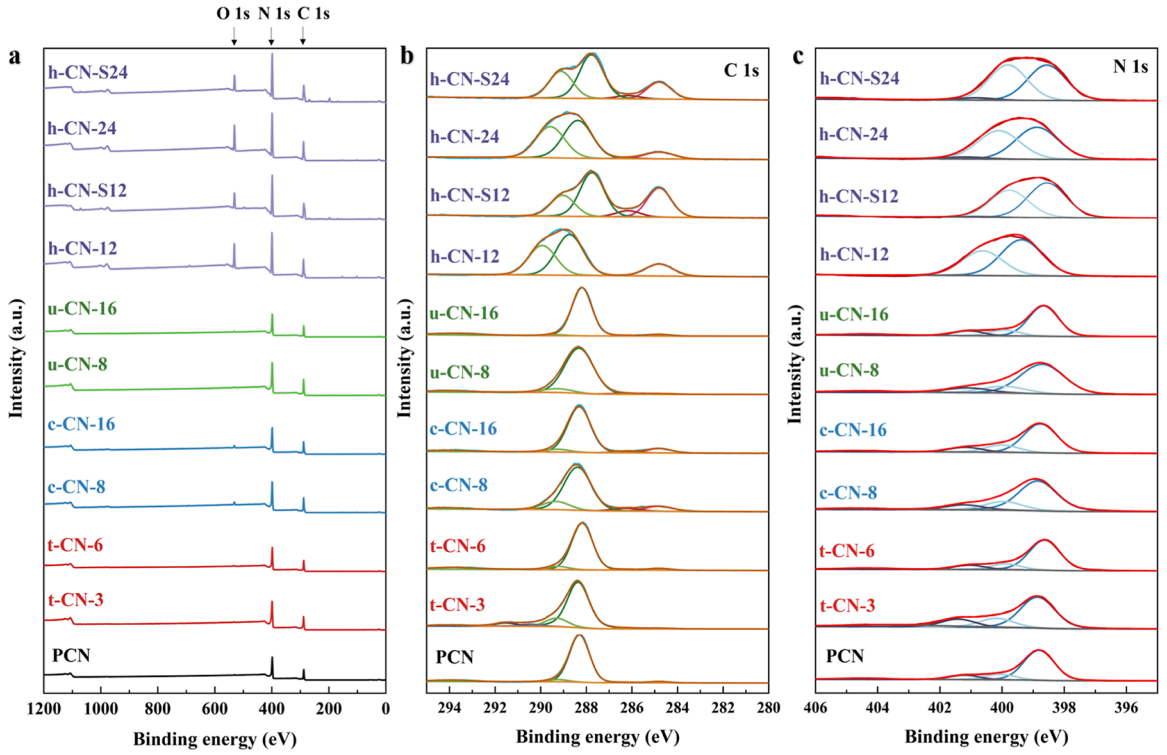

Figure 6. XPS survey spectra (a) and high-resolution XPS spectra of C1s (b) and N1s (c) of differently exfoliated PCN.

all other exfoliated samples did not increase as desired and even badly decreased.

Crystal Structure, Surface Group, and Structural Defects. Powder X-ray diffraction (XRD) was conducted to identify the present phases and gain insights into their crystal structures. For u-CN (Figure 5a), the positions and intensities of the main diffraction reflexes are similar to those of pristine PCN, indicating that the original crystal structure of PCN is well retained. The strong (002) reflex at 27.7° and weak (210) reflex at 12.8° are attributed to the interlayer $\pi-\pi$ stacking structure of heptazine units (C_6N_7) and in-planar repeats between heptazine units, respectively.[31,32] However, the relative intensity of the (002) reflex of c-CN becomes weaker and broader and its (210) reflex is missing. These changes demonstrate that the crystallite size along the (002) direction is decreasing and the lattice-like structure along the (210) direction is disappearing, providing evidence of exfoliation. In contrast, the (002) reflex intensity for t-CN becomes significantly higher than that of pristine PCN due to its increased crystallinity.[33] The most significant change occurred in the h-CN samples. For h-CN-12 and h-CN-24, the intensities of the (002) reflex decrease over time, and the (210) reflex disappears and is replaced by a new and sharp reflex at 10.7°, proving the complete decomposition of PCN by the time applying high pressure and temperature and conversion into a new compound. The newly formed compound was assigned to the supramolecular derivatives, which is a complex of melamine and cyanuric acid, containing hydrogen bonding.[6,34] With respect to the soluble samples h-CN-S12 and h-CN-S24, the diffraction reflexes were indexed to the melamine.[35] Therefore, it is certain that the hydrothermal treatment has a significant decomposition effect on the crystal structure of PCN and thus possibly destroys its π-delocalized electronic system. Consequently, the photocatalytic activity could be lost. On the basis of XRD analysis, we conclude that the 2D conjugated structures of PCN are well maintained after liquid ultrasonic exfoliation, while thermal oxidation and chemical oxidation strongly affect the crystal structure of PCN. Certainly, the most destructive method is hydrothermal oxidation.

The potential change in molecular structure was evaluated by DRIFTS. As depicted in Figure 5b, the characteristic DRIFTS spectra of t-CN and u-CN closely resemble those of the pristine PCN, suggesting that the original PCN backbone remained the same. The broad peak at 3500−3000 cm^{-1} is assigned to the stretching modes of the N−H, N−H_2, and O−H stretches.[36−38] The strong bands in 1700−1200 cm^{-1} correspond to the stretching and bending modes of the heptazine heterocyclic ring. The sharper band at 821 cm^{-1} belongs to the typical heptazine breathing mode.[39] However, upon chemical oxidation exfoliation, c-CN exhibits a broadened band in 3500−3000 cm^{-1} due to the increase in oxygen-containing groups, as further confirmed by CHNS and XPS elemental analysis (Table S2). At the same time, the weakened peaks in 1700−1200 and 821 cm^{-1} indicate the partial fracture of heptazine units after treatment with H_2SO_4, leading to a less ordered in-plane structural packing motif.[27,35] Obviously, the molecular structures of h-CN-12 and h-CN-24 are no longer identical to PCN, aligning with the observation of XRD. The newly emerged band at 1794 cm^{-1} is attributed to the formation of carbonyl groups. In h-CN-S12 and h-CN-S24, we observed discernible and additional absorption peaks of melamine. Specifically, the two distinct bands at 3471 and 3426 cm^{-1} are assigned to the stretching vibrations of the N−H in the terminal amine group. The band at 782 cm^{-1} is the typical absorption of the melamine structure, attributed to the bending and stretching vibrations of C−N heterocycles.[35]

XPS was used to further probe the changes in the chemical states of C, N, and O. As displayed in the survey spectra (Figure 6a), the relative intensities of the O 1s atoms for c-CN

https://doi.org/10.1021/acsanm.4c00133
ACS Appl. Nano Mater. XXXX, XXX, XXX−XXX

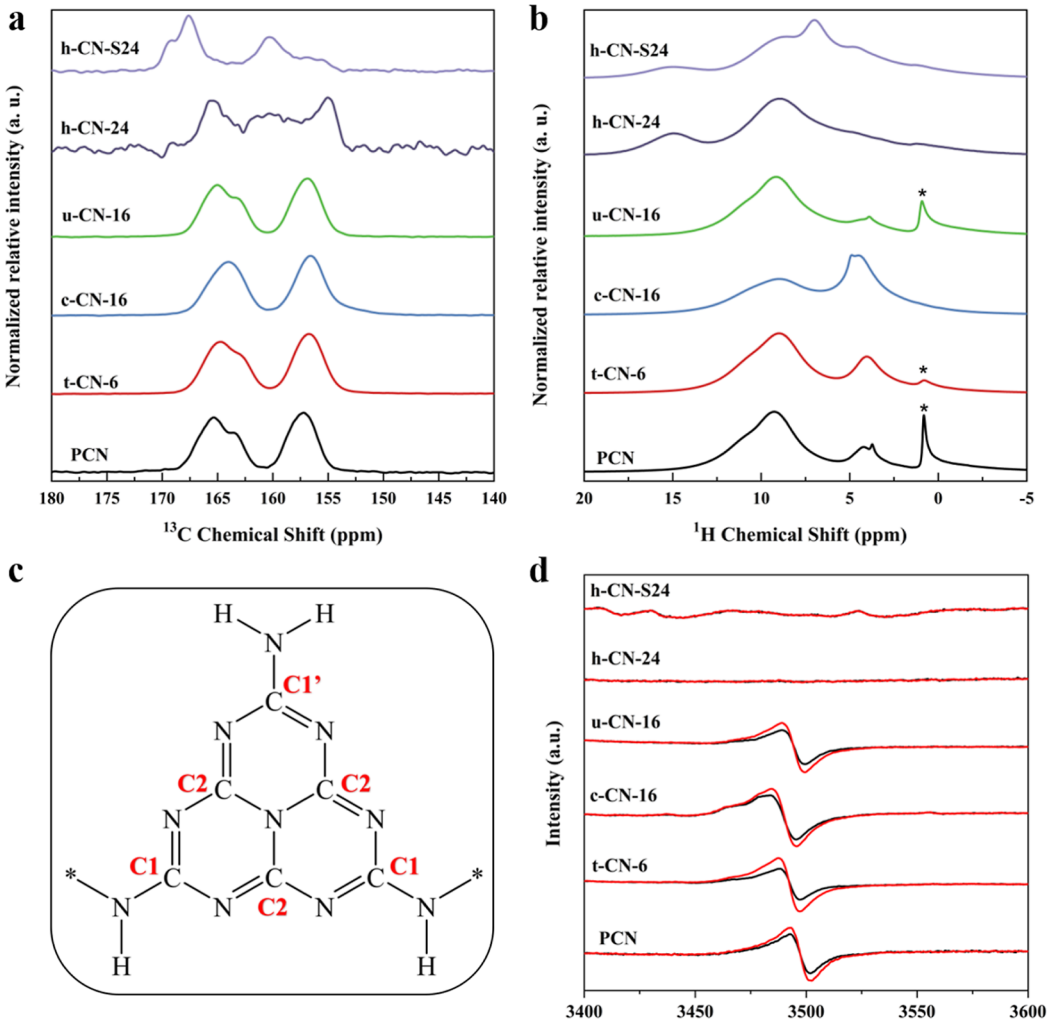

Figure 7. (a) ^{13}C CPMAS NMR spectra at 8 kHz, recorded with the near-quantitative multi-CP sequence,[47] and (b) ^{1}H MAS NMR at 60 kHz rotational frequency of differently exfoliated PCN. * Mark an impurity signal from isopropanol. (c) Chemical structures of heptazine unit. * Atomic connectivity to the next heptazine unit. (d) EPR spectra of differently exfoliated PCN with (red line) and without (black line) the light (>420 nm) irradiation.

and h-CN were much stronger than that of pristine PCN, especially for h-CN, confirming the presence of a higher concentration of surface O atoms within the material. The high-resolution C 1s spectrum (Figure 6b) of pristine PCN, ranging from 281.8 to 298.1 eV, was resolved into four peaks located at 289.8, 288.3, 286.4, and 284.6 eV, assigned to N═C−O, N−C═N, N−$(C)_3$, and C−C bonds, respectively.[40,41] For h-CN-12 and h-CN-24, the binding energy of N═C−N is positively shifted compared to that of pristine PCN due to the introduction of O atoms with higher electronegativity in the aromatic CN heterocycles (Allen electronegativity: O = 3.6, N = 3.1, C = 2.5). Additionally, the relative peak area of N═C−O for t-CN-3 and c-CN-8 is significantly larger than pristine PCN, whereas N═C−N is smaller (Table S3). This result is reasonable because part of the N═C−N was oxidized to the N═C−O. The loss of nitrogen atoms was further confirmed by comparing the surface C/N atomic ratios before and after the treatments. The surface C/N atomic ratios for c-CN-16 and t-CN-6 increased to 0.82 and 0.80 (Table S2), respectively, which are higher than that of pristine PCN of 0.70. The decrease in N content and the increase in the level of O content confirmed that the aromatic CN heterocycles were oxidized during the thermal and chemical treatments.

For the N 1s XPS spectrum, there are no obvious binding energy shifts of N 1s core electrons in t-CN, c-CN, and u-CN. The large peak, ranging from 396.4 to 402.7 eV, can be deconvoluted into three peaks (Figure 6c). The peaks at binding energies of 398.8, 400.1, and 401.2 eV correspond to the sp^2 C═N−C bonds in the tri-*s*-triazine (pyridinic N), sp^3 tertiary nitrogen N−$(C)_3$ groups, and amino functions carrying hydrogen (C−N−H), respectively.[42] The small peak located at 404.6 eV is attributed to the charging effect or π electrons delocalization in heterocycles.[43] For h-CN-12, the binding energies of C−N−H and N−$(C)_3$ are all positively shifted (Table S4). In contrast, the binding energies of C−N−H, N−$(C)_3$, and C═N−C in h-CN-S12 are all negatively shifted. Such binding energy shift of N 1s and C 1s core electrons in h-CN-12 and h-CN-S12 is caused by the decomposition of the heptazine unit and the introduction of surface oxygen-containing groups.[9,44]

Solid-state nuclear magnetic resonance (NMR) spectroscopy was employed to further elucidate the compositional and structural changes in the exfoliated samples. In the ^{13}C NMR spectrum (Figure 7a), two peaks appeared at about 165 ppm (C1/C1′) and 157 ppm (C2), corresponding to heptazine units (Figure 7c) and in agreement with a previous report.[45]

https://doi.org/10.1021/acsanm.4c00133
ACS Appl. Nano Mater. XXXX, XXX, XXX−XXX

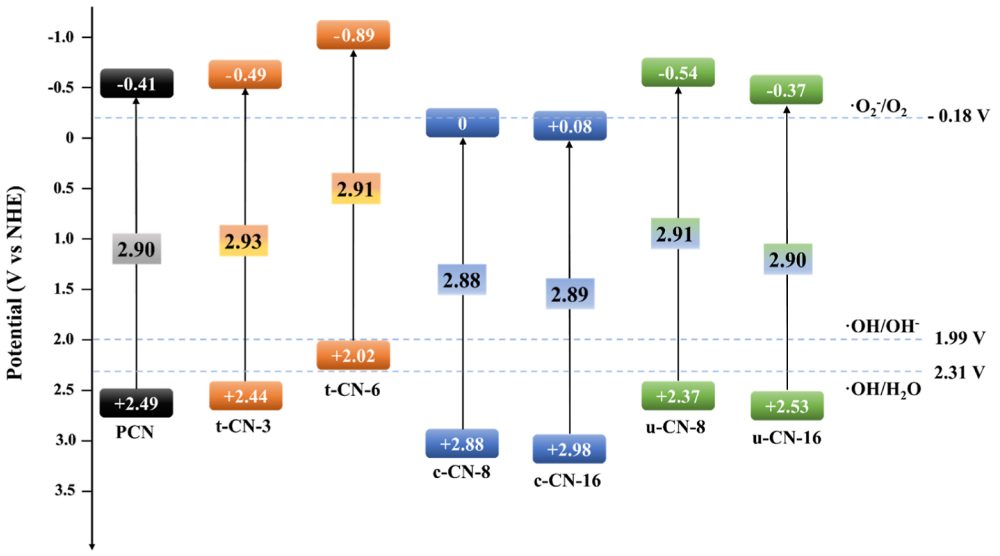

Figure 8. Electronic band structure of differently exfoliated PCN.

The signal at 163−165 ppm can be further divided into two carbon environments: the carbon atom near an NH_2 group (C1′ at 165 ppm) and the carbon atom near a bridging −NH− nitrogen atom (C1 at 163 ppm). Another signal at 157 ppm (C2) is assigned to carbon atoms that are bonded to three non-hydrogen-carrying nitrogen atoms. The presence of two ^{13}C NMR signals in t-CN-6, c-CN-16, and u-CN-16 is consistent with that of PCN, indicating the maintenance of heptazine units. The shift of the center of weight of the C1/C1′ peak in c-CN-16 is attributed to a relative increase in the C1 (R_2−NH) contribution, suggesting that the edge $-NH_2$ group was destroyed. The h-CN-24 and h-CN-S24 have different spectral fingerprints, indicating that partial oxidation of the aromatic system could lead to deshielding (downfield shift). Specifically, the observed two signals in h-CN-S24 at 167.6 and 169.3 ppm suggest the formation of a melamine structure.[46] Additional evidence of the modification of PCN comes from ^1H MAS NMR spectra (Figure 7b). The profiles are similar, with the main features at 9.2 and 4.2 ppm; the former is assigned to the hydrogen-bonded NH_2 group, and the latter is assigned to NH_2 substituents lacking hydrogen bonds. The increased peak intensity at 5 ppm in c-CN-16 can be assigned to the OH groups arising from the oxidation of heptazine units. The significantly lower intensity of the peak at 9 ppm indicates the decrease of the edge $-NH_2$ group, consistent with the observation from ^{13}C MAS NMR spectra. The signal appearing at about 7 ppm in the spectra of h-CN-S24 is attributed to NH_3^+, which could explain its water solubility. The peak at 15 ppm in the spectra of h-CN-S24 could point to the presence of keto-imines, originating from the oxidation of melamine. This tentative keto-imine peak was also observed in h-CN-24, which provides further support for the formation of supramolecular complexes.

Further evidence of structural changes in the exfoliated PCN was obtained by in situ EPR spectroscopy. As shown in Figure 7d, an EPR signal with a g value of 2.0038 was observed in PCN, t-CN-6, c-CN-16, and u-CN-16. This signal is attributed to the unpaired electrons on the sp^2-carbon atoms inside the π-conjugated C_3N_4 network.[48] With further visible light irradiation, an enhanced EPR signal was found, suggesting the generation of more free electrons as a result of the light irradiation.[49] However, in h-CN-24 and h-CN-S24, this signal is not present, indicating the absence of free charge carriers due to decomposition of the π-conjugated C_3N_4 network.

Optical and Electronic Properties. The optical absorption properties of the exfoliated PCN were investigated by UV−vis DRS. As shown in Figure S10, there are no obvious shifts of light absorption edges in t-CN, c-CN, and u-CN compared to pristine PCN. However, evaluation of the spectra of h-CN revealed an apparent decrease in absorbance and a blue-shift in absorption edge over time. The corresponding optical bandgaps of pristine PCN and exfoliated PCN were estimated from the Tauc plot,[50] as shown in Figure S10c. In combination with the flat band potential (versus Ag/AgCl at pH 6.6), this potential was estimated by Mott−Schottky plots (Figure S11), and the electronic band structures of exfoliated PCN are calculated and illustrated in Figure 8. We found that the highest occupied molecular orbital (HOMO) potential of t-CN exhibits an upward shift with increasing exfoliation time. Conversely, the HOMO potential of c-CN shows a downward trend. The HOMO and lowest unoccupied molecular orbital potentials (LUMO) of u-CN are considered the same as pristine PCN.

The shift trends of the valence band (VB) edge in t-CN and c-CN were further proven by VB XPS spectra (Figure S12). The VB potential of t-CN-6 is 2.56 eV, which shows a noticeable upshift compared to pristine PCN (2.67 eV). On the contrary, the VB edge of c-CN shifted progressively downward with increasing exfoliation time. Thus, chemical exfoliation could result in a downward shift in the potential of VB and CB edges. The resulting c-CN possesses a higher thermodynamic driving force for photooxidation reactions of the photogenerated holes but weakens the photoreduction ability of electrons. In contrast, thermal exfoliation could lead to the potential of VB and CB edges of PCN upward, thus improving the photoreduction ability of electrons but reducing the photooxidation ability of holes. Due to the lack of free charge carriers in h-CN (confirmed by EPR), its band structure is not discussed.

Charge-Carrier Separation and Transport. Photocurrent response was performed to evaluate the charge transfer behaviors (Figure 9a). It is generally acknowledged that the

https://doi.org/10.1021/acsanm.4c00133
ACS Appl. Nano Mater. XXXX, XXX, XXX−XXX

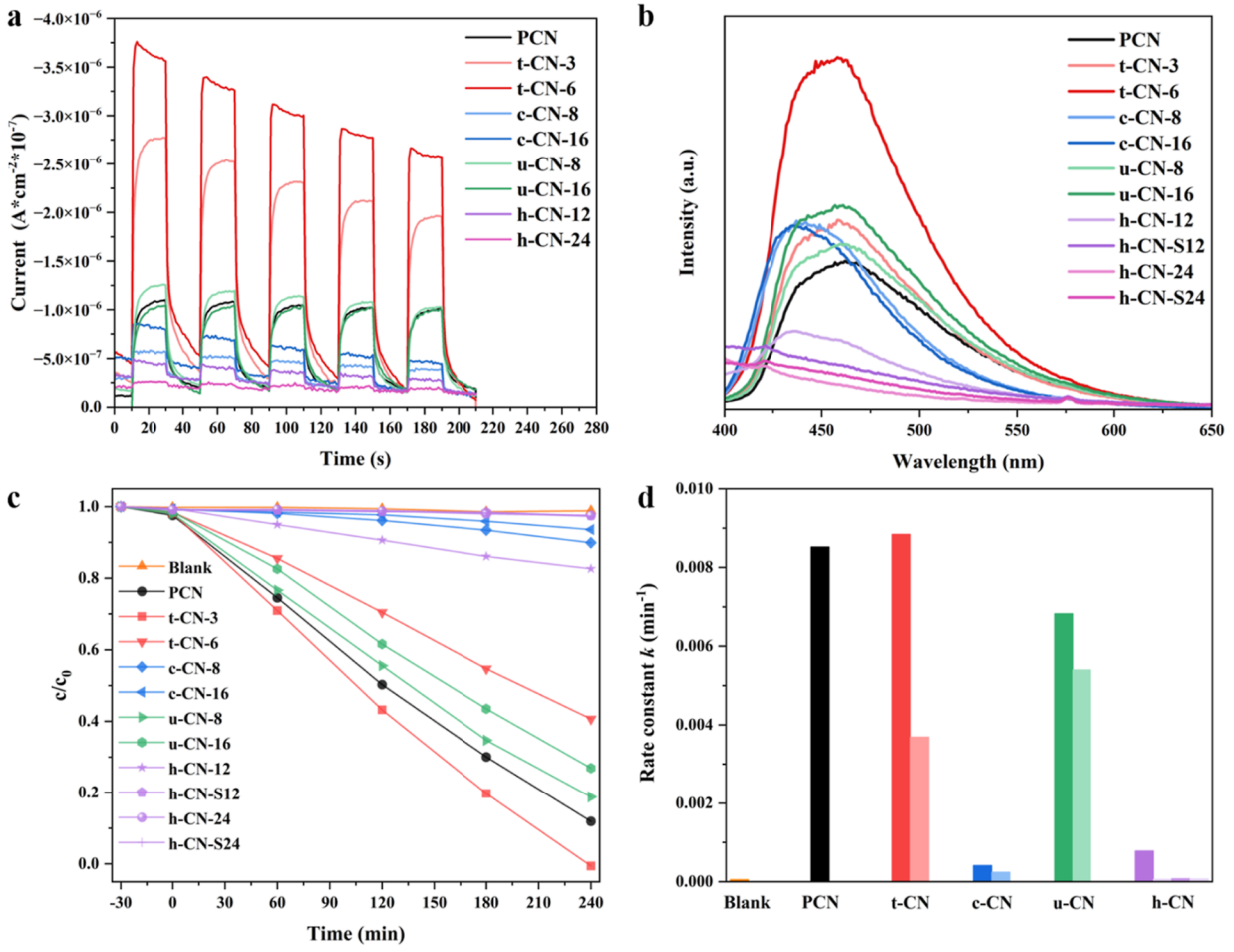

Figure 9. (a) Transient photocurrent ($I-T$) curves and (b) PL (emission) spectra of differently exfoliated PCN. (c) Photocatalytic activity and (d) pseudo-first-order rate constants of phenol degradation with differently exfoliated PCN.

higher photocurrent intensity means elevated photoelectric conversion efficiency.[51] In comparison with pristine PCN, the photocurrent intensity remains the same in u-CN, while a significant drop in intensity is observed in c-CN and h-CN. This suggests that the generation of photoexcited electrons is suppressed after chemical and hydrothermal treatments. Conversely, we observed a considerable enhancement in photocurrent with increasing exfoliation time in t-CN, suggesting a higher light utilization efficiency compared to pristine PCN.[52] The photocurrent density of t-CN-6 was about 2 times higher than that of pristine PCN. Notably, under light irradiation, the photocurrent of t-CN-3 gradually increased until reaching its maximum. A similar photocurrent curve is also observed in pristine PCN and u-CN. In contrast, for t-CN-6, the initial illumination produced a large photocurrent and then dropped to form a small spike, which might be due to the rapid recombination of photoinduced electron−hole pairs.[5]

Figure 9b shows the photoluminescence (PL) spectra of the differently exfoliated PCN. Upon excitation at 365 nm, the PCN generates a PL spectrum in the range of 400−650 nm, with a main emission peak at 468 nm. All t-CN, c-CN, and u-CN show an enhanced PL intensity compared to that of pristine PCN, and their intensities further increase over the exfoliation time. This indicates the suppressed separation efficiency of charge carrier after exfoliation.[17,20] Thus, thermal exfoliation promoted the generation of photoexcited electrons but also resulted in a high charge-carrier recombination. In addition, c-CN exhibits a blue-shift of 30 nm due to the quantum confinement effect caused by the decreased size.[23] Same as the above photocurrent analysis, due to the low charge-carrier generation, a weak PL signal was observed in h-CN.

Photocatalytic Performance and Mechanism. The visible-light photodegradation of phenol was used to determine the activity of the exfoliated PCN samples. The reaction kinetics are modeled by the pseudo-first-order kinetics model: $\ln(c/c_0) = -kt$, where c_0 and c are the initial concentration and instant concentration at reaction time t, and k is the rate constant. As shown in Figure 9c,d, t-CN-3 shows the highest rate constant (0.0088 min^{-1}), which is the one higher than the pristine PCN (0.0085 min^{-1}). However, the rate constant of t-CN-6 is decreased to 0.0037 min^{-1}, which is only half that of t-CN-3. The decreased activity might be due to the high electron−hole recombination rate, pointing out the negative effects of excessive exfoliation. A similar trend was observed in the c-CN, u-CN, and h-CN samples. It is worth mentioning here that in our test, the t-CN and u-CN are still highly active for the reaction, while for c-CN and h-CN, the activity is reduced by 90%, which is due to their low surface area and poor generation rate of photoexcited electrons.

To understand the mechanism of phenol photodegradation, we performed DMPO spin-trapping EPR measurements. It is known that the EPR can be used to verify the formation of reactive radicals. As illustrated in Figure S16, the distinguish-

https://doi.org/10.1021/acsanm.4c00133
ACS Appl. Nano Mater. XXXX, XXX, XXX−XXX

able DMPO-OH was detected in pristine PCN, indicating the formation of ·OH radicals under visible-light irradiation. The HOMO level of PCN is 2.49 V (vs NHE), which is more positive than those of ·OH/OH^- (1.99 V vs NHE) and ·OH/H_2O (2.31 V vs NHE), and the production of ·OH is allowed. However, the ·OH radical generation ability in c-CN-16 and u-CN-16 has deteriorated. Instead, the signal of photoexcited electrons from VB to CB in the bulk can be observed, indicating that the electrons are mostly captured by the bulk, and only a few electrons are able to reach the surface and react with H_2O to generate the ·OH radical. Similarly, the ·OH signal intensity in t-CN-6 slightly decreased compared to pristine PCN. This decrease is caused by the fast recombination of charge carriers in the bulk. For the best-performing sample t-CN-3, except for the $^{\bullet}OH$ radical, an additional $^{\bullet}O_2^-$ radical was observed (Figure S17). Accordingly, the related flat band potential of t-CN-3 is −0.49 V (vs NHE), which is more negative than the standard potential of $O_2/^{\bullet}O_2^-$ (−0.18 V vs NHE), and thereby $^{\bullet}O_2^-$ can be thermodynamically generated.

CONCLUSIONS

In summary, the PCN nanosheets prepared by four different exfoliation methods exhibit varying morphologies and band structures. Our approach of not separating different fractions of the exfoliated product allowed us to unravel the mechanisms by which the size reduction occurs. While it has been anticipated that exfoliation is necessarily associated with partial destruction of the internal order in the pristine PCN, there are surprising deviations between the various exfoliation methods. The hydrothermal route destroyed the extended structure almost completely, leading to the formation of melamine units and hardly any retained semiconductor properties. Chemical exfoliation retains the semiconducting properties of the PCN; however, a decreased performance is observed due to disruption of the original porous structure. Thermal and ultrasonic exfoliation methods demonstrated effectiveness in reducing the thickness of PCN while preserving the original structure. Notably, only the thermally exfoliated PCN exhibited better activity than the pristine PCN, and controlling the exfoliation time is vital. The negative shift of the band edges and the additional formation of superoxide radicals may play a decisive role here. It is important to note that always two processes will occur during the exfoliation process that affect the PCN structure: one is to overcome the interlayer van der Waals forces, and the other is the rupture of in-plane hydrogen bonds. Therefore, the preparation of PCN nanosheets without any fragmentation remains a great challenge. This work provides a comprehensive understanding of PCN exfoliation, which would serve as valuable guidance for the future design of PCN nanosheets for photocatalytic applications.

ASSOCIATED CONTENT

Supporting Information

The Supporting Information is available free of charge at https://pubs.acs.org/doi/10.1021/acsanm.4c00133.

Detail of materials synthesis, materials characterization, DFT calculation, and photocatalytic experiment; additional computational and experimental data, including interlayer energy, hydrogen bond energy, TGA−MS, DRIFTS, SEM, AFM, N_2 adsorption−desorption isotherms, UV−vis adsorption spectra, Mott−Schottky plots, VB-XPS spectra, EPR spectra, elemental analysis; discussion of the presented work and literature results, apparent density, density of state, and production yield (PDF)

AUTHOR INFORMATION

Corresponding Author

Jennifer Strunk − *Leibniz Institute for Catalysis e.V., 18059 Rostock, Germany; Industrial Chemistry and Heterogeneous Catalysis, Technical University of Munich, 85748 Garching, Germany;* orcid.org/0000-0002-6018-3633; Email: jennifer.strunk@catalysis.de

Authors

Junhao Huang − *Leibniz Institute for Catalysis e.V., 18059 Rostock, Germany*

Marcus Klahn − *Leibniz Institute for Catalysis e.V., 18059 Rostock, Germany*

Xinxin Tian − *Institute of Molecular Science, Key Laboratory of Materials for Energy Conversion and Storage of Shanxi Province, Key Laboratory of Chemical Biology and Molecular Engineering of Education Ministry, Shanxi University, Taiyuan 030006, China;* orcid.org/0000-0002-3195-3176

Xingchao Dai − *Leibniz Institute for Catalysis e.V., 18059 Rostock, Germany*

Jabor Rabeah − *Leibniz Institute for Catalysis e.V., 18059 Rostock, Germany;* orcid.org/0000-0003-2162-0981

Victoria Aladin − *Institute of Chemistry, Faculty of Mathematics and Natural Sciences, University of Rostock, 18059 Rostock, Germany; Department Life, Light & Matter, Faculty for Interdisciplinary Research, University of Rostock, 18059 Rostock, Germany*

Björn Corzilius − *Leibniz Institute for Catalysis e.V., 18059 Rostock, Germany; Institute of Chemistry, Faculty of Mathematics and Natural Sciences, University of Rostock, 18059 Rostock, Germany; Department Life, Light & Matter, Faculty for Interdisciplinary Research, University of Rostock, 18059 Rostock, Germany;* orcid.org/0000-0003-3937-9137

Stephan Bartling − *Leibniz Institute for Catalysis e.V., 18059 Rostock, Germany;* orcid.org/0000-0001-5901-7235

Henrik Lund − *Leibniz Institute for Catalysis e.V., 18059 Rostock, Germany;* orcid.org/0000-0001-7747-2178

Norbert Steinfeldt − *Leibniz Institute for Catalysis e.V., 18059 Rostock, Germany;* orcid.org/0000-0003-0491-6481

Tim Peppel − *Leibniz Institute for Catalysis e.V., 18059 Rostock, Germany;* orcid.org/0000-0002-7814-7235

Andrew J. Logsdail − *Max Planck−Cardiff Centre on the Fundamentals of Heterogeneous Catalysis (FUNCAT), Cardiff Catalysis Institute, School of Chemistry, Cardiff University, Cardiff CF10 3AT, U.K.;* orcid.org/0000-0002-2277-415X

Haijun Jiao − *Leibniz Institute for Catalysis e.V., 18059 Rostock, Germany;* orcid.org/0000-0002-2947-5937

Complete contact information is available at: https://pubs.acs.org/10.1021/acsanm.4c00133

Notes

The authors declare no competing financial interest.

https://doi.org/10.1021/acsanm.4c00133
ACS Appl. Nano Mater. XXXX, XXX, XXX−XXX

■ ACKNOWLEDGMENTS

The MAS NMR spectrometer at the University of Rostock has been funded by Deutsche Forschungsgemeinschaft (DFG, through grant INST 264/129-1). The authors thank the colleagues from the Analytical Services Group in LIKAT: Reinhard Eckelt for the sorption measurements, Astrid Lehmann for the elemental analysis, Christine Rautenberg for the thermogravimetry measurements, and Michael Sebek for the advice on ultrasonic experiments.

■ REFERENCES

(1) Ou, H.; Lin, L.; Zheng, Y.; Yang, P.; Fang, Y.; Wang, X. Tri-s-triazine-Based Crystalline Carbon Nitride Nanosheets for an Improved Hydrogen Evolution. *Adv. Mater.* **2017**, *29* (22), 1700008.
(2) Li, X.; Zhang, J.; Huo, Y.; Dai, K.; Li, S.; Chen, S. Two-dimensional sulfur- and chlorine-codoped g-C_3N_4/CdSe-amine heterostructures nanocomposite with effective interfacial charge transfer and mechanism insight. *Appl. Catal., B* **2021**, *280*, 119452.
(3) Fu, J.; Zhu, B.; Jiang, C.; Cheng, B.; You, W.; Yu, J. Hierarchical Porous O-Doped g-C_3N_4 with Enhanced Photocatalytic CO_2 Reduction Activity. *Small* **2017**, *13* (15), 1603938.
(4) Wang, K.; Li, Q.; Liu, B.; Cheng, B.; Ho, W.; Yu, J. Sulfur-doped g-C_3N_4 with enhanced photocatalytic CO_2-reduction performance. *Appl. Catal., B* **2015**, *176*−*177*, 44−52.
(5) Li, X.; Zhang, J.; Wang, Z.; Fu, J.; Li, S.; Dai, K.; Liu, M. Interfacial C-S Bonds of g-C_3N_4/$Bi_{19}Br_3S_{27}$ S-Scheme Heterojunction for Enhanced Photocatalytic CO_2 Reduction. *Chem.—Eur. J.* **2023**, *29* (4), No. e202202669.
(6) Guo, S.; Deng, Z.; Li, M.; Jiang, B.; Tian, C.; Pan, Q.; Fu, H. Phosphorus-Doped Carbon Nitride Tubes with a Layered Micro-nanostructure for Enhanced Visible-Light Photocatalytic Hydrogen Evolution. *Angew. Chem., Int. Ed.* **2016**, *55* (5), 1830−1834.
(7) Chang, M.; Pan, Z.; Zheng, D.; Wang, S.; Zhang, G.; Anpo, M.; Wang, X. Salt-Melt Synthesis of Poly Heptazine Imides with Enhanced Optical Absorption for Photocatalytic Hydrogen Production. *ChemSusChem* **2023**, *16* (13), No. e202202255.
(8) Wang, Q.; Zhang, G.; Xing, W.; Pan, Z.; Zheng, D.; Wang, S.; Hou, Y.; Wang, X. Bottom-up Synthesis of Single-Crystalline Poly (Triazine Imide) Nanosheets for Photocatalytic Overall Water Splitting. *Angew. Chem., Int. Ed. Engl.* **2023**, *62* (37), No. e202307930.
(9) Ming, L.; Yue, H.; Xu, L.; Chen, F. Hydrothermal synthesis of oxidized g-C_3N_4 and its regulation of photocatalytic activity. *J. Mater. Chem. A* **2014**, *2* (45), 19145−19149.
(10) Yan, S. C.; Li, Z. S.; Zou, Z. G. Photodegradation performance of g-C_3N_4 fabricated by directly heating melamine. *Langmuir* **2009**, *25* (17), 10397−10401.
(11) Jun, Y.-S.; Lee, E. Z.; Wang, X.; Hong, W. H.; Stucky, G. D.; Thomas, A. From Melamine-Cyanuric Acid Supramolecular Aggregates to Carbon Nitride Hollow Spheres. *Adv. Funct. Mater.* **2013**, *23* (29), 3661−3667.
(12) Ghosh, I.; Khamrai, J.; Savateev, A.; Shlapakov, N.; Antonietti, M.; Konig, B. Organic semiconductor photocatalyst can bifunctionalize arenes and heteroarenes. *Science* **2019**, *365* (6451), 360−366.
(13) She, X.; Xu, H.; Xu, Y.; Yan, J.; Xia, J.; Xu, L.; Song, Y.; Jiang, Y.; Zhang, Q.; Li, H. Exfoliated graphene-like carbon nitride in organic solvents: enhanced photocatalytic activity and highly selective and sensitive sensor for the detection of trace amounts of Cu^{2+}. *J. Mater. Chem. A* **2014**, *2* (8), 2563−2570.
(14) Ran, J.; Ma, T. Y.; Gao, G.; Du, X.-W.; Qiao, S. Z. Porous P-doped graphitic carbon nitride nanosheets for synergistically enhanced visible-light photocatalytic H_2 production. *Energy Environ. Sci.* **2015**, *8* (12), 3708−3717.
(15) Novoselov, K. S.; Mishchenko, A.; Carvalho, A.; Neto, A. H. C. 2D materials and van der Waals heterostructures. *Science* **2016**, *353* (6298), aac9439.
(16) Voiry, D.; Yang, J.; Kupferberg, J.; Fullon, R.; Lee, C.; Jeong, H. Y.; Shin, H. S.; Chhowalla, M. High-quality graphene via microwave reduction of solution-exfoliated graphene oxide. *Science* **2016**, *353* (6306), 1413−1416.
(17) Niu, P.; Zhang, L.; Liu, G.; Cheng, H.-M. Graphene-Like Carbon Nitride Nanosheets for Improved Photocatalytic Activities. *Adv. Funct. Mater.* **2012**, *22* (22), 4763−4770.
(18) Zhang, X.; Xie, X.; Wang, H.; Zhang, J.; Pan, B.; Xie, Y. Enhanced photoresponsive ultrathin graphitic-phase C_3N_4 nanosheets for bioimaging. *J. Am. Chem. Soc.* **2013**, *135* (1), 18−21.
(19) Wu, X.; Chen, F.; Wang, X.; Yu, H. In situ one-step hydrothermal synthesis of oxygen-containing groups-modified g-C_3N_4 for the improved photocatalytic H_2-evolution performance. *Appl. Surf. Sci.* **2018**, *427*, 645−653.
(20) Xu, J.; Zhang, L.; Shi, R.; Zhu, Y. Chemical exfoliation of graphitic carbon nitride for efficient heterogeneous photocatalysis. *J. Mater. Chem. A* **2013**, *1* (46), 14766−14772.
(21) Ma, L.; Fan, H.; Li, M.; Tian, H.; Fang, J.; Dong, G. A simple melamine-assisted exfoliation of polymeric graphitic carbon nitrides for highly efficient hydrogen production from water under visible light. *J. Mater. Chem. A* **2015**, *3* (44), 22404−22412.
(22) Yang, P.; Ou, H.; Fang, Y.; Wang, X. A Facile Steam Reforming Strategy to Delaminate Layered Carbon Nitride Semiconductors for Photoredox Catalysis. *Angew. Chem., Int. Ed.* **2017**, *56* (14), 3992−3996.
(23) Ji, J.; Wen, J.; Shen, Y.; Lv, Y.; Chen, Y.; Liu, S.; Ma, H.; Zhang, Y. Simultaneous Noncovalent Modification and Exfoliation of 2D Carbon Nitride for Enhanced Electrochemiluminescent Biosensing. *J. Am. Chem. Soc.* **2017**, *139* (34), 11698−11701.
(24) Zhang, M.; Yang, Y.; An, X.; Zhao, J.; Bao, Y.; Hou, L. A. Exfoliation method matters: The microstructure-dependent photoactivity of g-C_3N_4 nanosheets for water purification. *J. Hazard. Mater.* **2022**, *424*, 127424.
(25) Schwinghammer, K.; Mesch, M. B.; Duppel, V.; Ziegler, C.; Senker, J.; Lotsch, B. V. Crystalline carbon nitride nanosheets for improved visible-light hydrogen evolution. *J. Am. Chem. Soc.* **2014**, *136* (5), 1730−1733.
(26) Feng, C.; Wu, Z. P.; Huang, K. W.; Ye, J.; Zhang, H. Surface Modification of 2D Photocatalysts for Solar Energy Conversion. *Adv. Mater.* **2022**, *34* (23), No. e2200180.
(27) Cheng, F.; Wang, H.; Dong, X. The amphoteric properties of g-C_3N_4 nanosheets and fabrication of their relevant heterostructure photocatalysts by an electrostatic re-assembly route. *Chem. Commun.* **2015**, *51* (33), 7176−7179.
(28) Villalobos, L. F.; Vahdat, M. T.; Dakhchoune, M.; Nadizadeh, Z.; Mensi, M.; Oveisi, E.; Campi, D.; Marzari, N.; Agrawal, K. V. Large-scale synthesis of crystalline g-C_3N_4 nanosheets and high-temperature H_2 sieving from assembled films. *Sci. Adv.* **2020**, *6* (4), No. eaay9851.
(29) Zhang, Y.; Liu, J.; Wu, G.; Chen, W. Porous graphitic carbon nitride synthesized via direct polymerization of urea for efficient sunlight-driven photocatalytic hydrogen production. *Nanoscale* **2012**, *4* (17), 5300−5303.
(30) Kessler, F. K.; Zheng, Y.; Schwarz, D.; Merschjann, C.; Schnick, W.; Wang, X.; Bojdys, M. J. Functional carbon nitride materials — design strategies for electrochemical devices. *Nat. Rev. Mater.* **2017**, *2* (6), 17030.
(31) Zhuo, H. Y.; Zhang, X.; Liang, J. X.; Yu, Q.; Xiao, H.; Li, J. Theoretical Understandings of Graphene-based Metal Single-Atom Catalysts: Stability and Catalytic Performance. *Chem. Rev.* **2020**, *120* (21), 12315−12341.
(32) Fina, F.; Callear, S. K.; Carins, G. M.; Irvine, J. T. S. Structural Investigation of Graphitic Carbon Nitride via XRD and Neutron Diffraction. *Chem. Mater.* **2015**, *27* (7), 2612−2618.
(33) Groenewolt, M.; Antonietti, M. Synthesis of g-C_3N_4 Nanoparticles in Mesoporous Silica Host Matrices. *Adv. Mater.* **2005**, *17* (14), 1789−1792.
(34) Dante, R. C.; Sánchez-Arévalo, F. M.; Chamorro-Posada, P.; Vázquez-Cabo, J.; Huerta, L.; Lartundo-Rojas, L.; Santoyo-Salazar, J.; Solorza-Feria, O. Supramolecular intermediates in the synthesis of

https://doi.org/10.1021/acsanm.4c00133
ACS Appl. Nano Mater. XXXX, XXX, XXX−XXX

polymeric carbon nitride from melamine cyanurate. *J. Solid State Chem.* **2015**, *226*, 170−178.
(35) Zhou, Z.; Wang, J.; Yu, J.; Shen, Y.; Li, Y.; Liu, A.; Liu, S.; Zhang, Y. Dissolution and liquid crystals phase of 2D polymeric carbon nitride. *J. Am. Chem. Soc.* **2015**, *137* (6), 2179−2182.
(36) Xia, P.; Zhu, B.; Yu, J.; Cao, S.; Jaroniec, M. Ultra-thin nanosheet assemblies of graphitic carbon nitride for enhanced photocatalytic CO_2 reduction. *J. Mater. Chem. A* **2017**, *5* (7), 3230−3238.
(37) Wang, W.; Yu, J. C.; Shen, Z.; Chan, D. K.; Gu, T. g-C_3N_4 quantum dots: direct synthesis, upconversion properties and photocatalytic application. *Chem. Commun.* **2014**, *50* (70), 10148−10150.
(38) Liu, G.; Zhao, G.; Zhou, W.; Liu, Y.; Pang, H.; Zhang, H.; Hao, D.; Meng, X.; Li, P.; Kako, T.; Ye, J. In Situ Bond Modulation of Graphitic Carbon Nitride to Construct p-n Homojunctions for Enhanced Photocatalytic Hydrogen Production. *Adv. Funct. Mater.* **2016**, *26* (37), 6822−6829.
(39) Alwin, E.; Koci, K.; Wojcieszak, R.; Zielinski, M.; Edelmannova, M.; Pietrowski, M. Influence of High Temperature Synthesis on the Structure of Graphitic Carbon Nitride and Its Hydrogen Generation Ability. *Mater.* **2020**, *13* (12), 2756.
(40) Ye, C.; Li, J.-X.; Li, Z.-J.; Li, X.-B.; Fan, X.-B.; Zhang, L.-P.; Chen, B.; Tung, C.-H.; Wu, L.-Z. Enhanced Driving Force and Charge Separation Efficiency of Protonated g-C_3N_4 for Photocatalytic O_2 Evolution. *ACS Catal.* **2015**, *5* (11), 6973−6979.
(41) Ye, L.; Wu, D.; Chu, K. H.; Wang, B.; Xie, H.; Yip, H. Y.; Wong, P. K. Phosphorylation of g-C_3N_4 for enhanced photocatalytic CO_2 reduction. *Chem. Eng. J.* **2016**, *304*, 376−383.
(42) Huang, J.; Meng, P.; Liu, X. Porous nanostructure and enhanced charge transfer in graphitic carbon nitride fabricated by polyoxometalate oxidation etching. *J. Alloys Compd.* **2019**, *805*, 654−662.
(43) Foy, D.; Demazeau, G.; Florian, P.; Massiot, D.; Labrugère, C.; Goglio, G. Modulation of the crystallinity of hydrogenated nitrogen-rich graphitic carbon nitrides. *J. Solid State Chem.* **2009**, *182* (1), 165−171.
(44) Wu, X.; Wang, X.; Wang, F.; Yu, H. Soluble g-C_3N_4 nanosheets: Facile synthesis and application in photocatalytic hydrogen evolution. *Appl. Catal., B* **2019**, *247*, 70−77.
(45) Li, X.; Sergeyev, I. V.; Aussenac, F.; Masters, A. F.; Maschmeyer, T.; Hook, J. M. Dynamic Nuclear Polarization NMR Spectroscopy of Polymeric Carbon Nitride Photocatalysts: Insights into Structural Defects and Reactivity. *Angew. Chem., Int. Ed.* **2018**, *57* (23), 6848−6852.
(46) Jurgens, B.; Irran, E.; Senker, J.; Kroll, P.; Muller, H.; Schnick, W. Melem (2,5,8-triamino-tri-s-triazine), an important intermediate during condensation of melamine rings to graphitic carbon nitride: synthesis, structure determination by X-ray powder diffractometry, solid-state NMR, and theoretical studies. *J. Am. Chem. Soc.* **2003**, *125* (34), 10288−10300.
(47) Johnson, R. L.; Schmidt-Rohr, K. Quantitative solid-state ^{13}C NMR with signal enhancement by multiple cross polarization. *J. Magn. Reson.* **2014**, *239*, 44−49.
(48) Yang, L.; Huang, J.; Shi, L.; Cao, L.; Yu, Q.; Jie, Y.; Fei, J.; Ouyang, H.; Ye, J. A surface modification resultant thermally oxidized porous g-C_3N_4 with enhanced photocatalytic hydrogen production. *Appl. Catal., B* **2017**, *204*, 335−345.
(49) Zhang, G.; Li, G.; Heil, T.; Zafeiratos, S.; Lai, F.; Savateev, A.; Antonietti, M.; Wang, X. Tailoring the Grain Boundary Chemistry of Polymeric Carbon Nitride for Enhanced Solar Hydrogen Production and CO_2 Reduction. *Angew. Chem., Int. Ed.* **2019**, *58* (11), 3433−3437.
(50) Zhang, L.; Ran, J.; Qiao, S. Z.; Jaroniec, M. Characterization of semiconductor photocatalysts. *Chem. Soc. Rev.* **2019**, *48* (20), 5184−5206.
(51) Tang, D.; Shao, C.; Jiang, S.; Sun, C.; Song, S. Graphitic C_2N_3: An Allotrope of g-C_3N_4 Containing Active Azide Pentagons as Metal-Free Photocatalyst for Abundant H_2 Bubble Evolution. *ACS Nano* **2021**, *15*, 7208−7215.
(52) Yang, Y.; Xu, D.; Wu, Q.; Diao, P. Cu_2O/CuO Bilayered Composite as a High-Efficiency Photocathode for Photoelectrochemical Hydrogen Evolution Reaction. *Sci. Rep.* **2016**, *6*, 35158.

https://doi.org/10.1021/acsanm.4c00133
ACS Appl. Nano Mater. XXXX, XXX, XXX−XXX